Measurement Science and Technology

100 year anniversary
Measurement Science and Technology

Comparison among feature tracking and more consolidated velocimetry image analysis techniques in a fully developed turbulent channel flow

To cite this article: Monica Moroni and Antonio Cenedese 2005 *Meas. Sci. Technol.* **16** 2307

View the article online for updates and enhancements.

You may also like

- Stochastic particle advection velocimetry (SPAV): theory, simulations, and proof-of-concept experiments
  Ke Zhou, Jiaqi Li, Jiarong Hong et al.
- A quantitative study of track initialization of the four-frame best estimate algorithm for three-dimensional Lagrangian particle tracking
  A Clark, N Machicoane and A Aliseda
- Study on the analogy between velocity and temperature fluctuations in the turbulent rotating channel flows
  Zixuan Yang, Guixiang Cui, Chunxiao Xu et al.

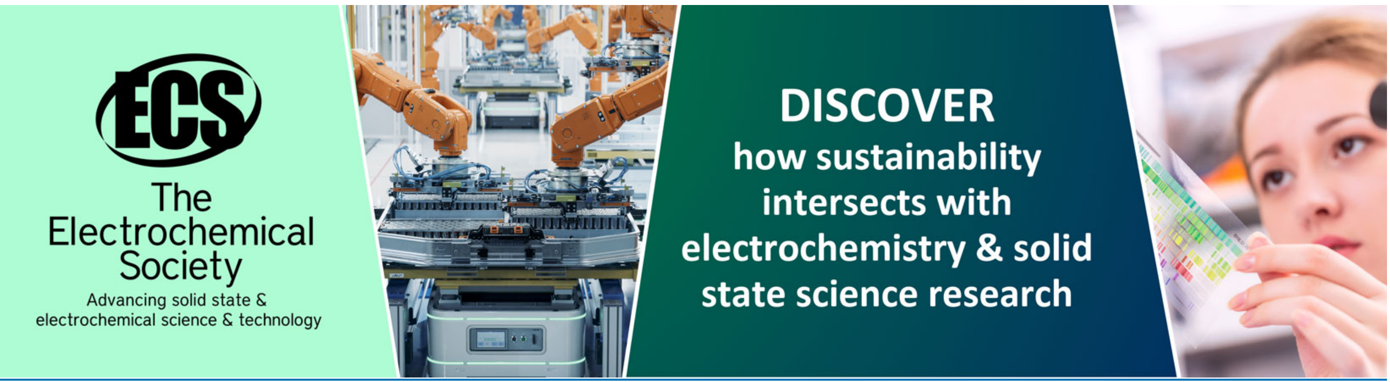

This content was downloaded from IP address 18.117.165.66 on 28/04/2024 at 01:45

INSTITUTE OF PHYSICS PUBLISHING MEASUREMENT SCIENCE AND TECHNOLOGY

Meas. Sci. Technol. **16** (2005) 2307–2322 doi:10.1088/0957-0233/16/11/025

Comparison among feature tracking and more consolidated velocimetry image analysis techniques in a fully developed turbulent channel flow

Monica Moroni[1] **and Antonio Cenedese**

Department of Hydraulics, Transportations and Roads, University of Rome 'La Sapienza', via Eudossiana 18, 00184 Rome, Italy

Received 11 April 2005, in final form 25 August 2005
Published 20 October 2005
Online at stacks.iop.org/MST/16/2307

Abstract
The presence of a large number of software codes for image analysis suggests the need for testing the suitability and accuracy of the algorithms developed. One of the possible approaches is testing these systems with experiments of well-known flow properties. Alternatively, tests can be performed by analysing synthetically generated images. The advantage of the latter approach is that there is no need to set up an experiment and the flow field is known in detail. This paper provides some insights into the relationship between results on both real and synthetic images in a turbulent channel flow. We focus on comparing performances of feature tracking, a novel image analysis technique, particle image velocimetry and particle tracking velocimetry. The three techniques have been used to explore first- and second-order statistics. The results are compared to direct numerical simulations of turbulent flow in a channel (Kim J, Moin P and Moser R 1987 Turbulence in channel flow at low Reynolds number *J. Fluid Mech.* **177** 133–66). Feature tracking performances are rather good, even in its purely translational motion model implementation. No constraints on tracer density have to be introduced. More than 3000 velocity vectors per frame were reconstructed. Resulting accuracy and resolution are always comparable to those achieved by the other techniques.

Keywords: turbulent channel flow, feature tracking, experiments, velocimetry image analysis techniques

1. Introduction

The fully developed turbulent boundary layer represents a widely analysed topic of fluid dynamics, from both an experimental and a numerical point of view. In experimental investigations, optical techniques (LDA (Romano 1995, Cenedese *et al* 1998); PIV (Liu *et al* 1991); 3-DPTV (Virant and Dracos 1997)) allow relevant results to be achieved by monitoring the flow field in the proximity of the wall in a non-invasive manner.

Particle imaging based techniques allowing multi-point velocity measurements are classified according to the density of tracer particles seeding the fluid:

- Low density images are generally approached from a Lagrangian point of view using particle tracking velocimetry (PTV) (Kobayashi *et al* 1989, Cenedese and Querzoli 1997, Cenedese *et al* 1997, among others). PTV provides sparse velocity vectors at points coincident with particle centroid positions.
- Medium-high particle density images are usually analysed by means of particle image velocimetry (PIV) (Adrian 1991, Westerweel 1998, Nogueira *et al* 2001, among others). PIV reconstructs the Eulerian velocity field on a regular, equi-spaced grid.

[1] Author to whom any correspondence should be addressed.

Particle tracking velocimetry is usually less extensively used but, compared to PIV, allows a larger spatial resolution (being able to detect regions very close to the walls) and an increased dynamic range. On the other hand, since seeding must be very sparse to ensure successful tracking, important features of turbulent flow may not be resolved even though each successful velocity measurement is highly localized.

This work compares the performances of PIV, PTV and a novel technique suitable for the estimation of the velocity field in any-density images, feature tracking (FT), which is well known in computer vision applications. FT reconstructs the displacement field by selecting image features (image portions suitable to be tracked because they remain almost unchanged for small time intervals) and tracking these from frame to frame. The matching measure used to follow a feature (and its interrogation window) and its 'most similar' region at successive times is the 'sum of squared differences' (SSD) among intensity values: the displacement is defined as the one that minimizes the SSD. In feature tracking, one applies the algorithm only to points where the solution for the displacement exists: those points are called 'good features to track' (Shi and Tomasi 1994).

Both PIV and FT use interrogation windows (an inner product of intensity values for the former and a distance measure—SSD—for the latter); PIV identifies the highest peak within the correlation matrix and FT solves a minimization problem. Few parameters are required to detect the displacement when the FT algorithm is employed. Those parameters may influence velocity vector density and accuracy but they do not force the displacements to accomplish user-defined constraints. In contrast, PTV algorithms need two parameters related to the maximum velocity and the acceleration within the flow field to be specified (Udrea *et al* 2000). Tracking of particles is performed by constraining the search of the same particle at subsequent times within limits described by the two parameters above.

The three techniques (PIV, PTV, FT) have been used to explore first- (mean) and second-order (variance and covariance) statistics of the velocity components in a fully developed turbulent channel flow. In particular, the following quantities have been investigated:

- $u+ = \frac{\bar{u}}{u^*}$, $v+ = \frac{\bar{v}}{u^*}$ (streamwise ($\bar{u}$) and normal ($\bar{v}$) mean velocity components);
- $u'+ = \sqrt{\frac{\sigma_u^2}{u^{*2}}}$, $v'+ = \sqrt{\frac{\sigma_v^2}{u^{*2}}}$ (turbulent intensities);
- $(u'v')+ = \sqrt{\frac{(u'v')^2}{u^{*2}}}$ (Reynolds stresses).

The quantities of interest are normalized using the friction velocity or the wall-shear velocity:

$$u^* = \sqrt{\tau_0/\rho}, \qquad (1)$$

where τ_0 is the shear stress at the wall. The empirical formula by Djenidi *et al* (1997) allows the computation of u^*:

$$u^* = \frac{U}{e^{\left(\frac{3}{2a}\right)}}\left[\frac{e^{\left(\frac{3}{2a}\right)}}{C}\right]^{\frac{1}{1+a}} = \frac{U}{e^{\frac{3}{2(1+a)}}\, C^{\frac{1}{1+a}}}, \qquad (2)$$

where U is the mean centreline velocity,

$$a = \frac{3}{2\ \ln(Re)}, \qquad C = \frac{\sqrt{3}+5a}{2a}. \qquad (3)$$

There are several reasons for this flow to be particularly challenging (Di Florio *et al* 2002):

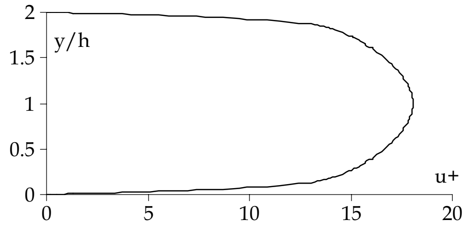

Figure 1. Mean velocity profile normalized by the wall-shear velocity.

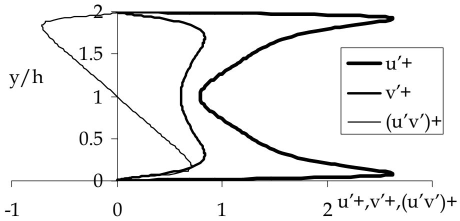

Figure 2. Turbulent intensities and Reynolds shear stresses normalized by the wall-shear velocity.

- large velocity gradients close to the wall may influence the precision and reliability of measurements;
- the finite size of non-ideal tracers may cause them to deviate from real motion near the wall;
- the reflection of laser light from the wall can seriously worsen the quality of measurements.

Several parameters are varied to test the precision and reliability of the computed statistics:

- seeding density;
- frame rate of the image sequence;
- Reynolds number;
- dimensions of the acquisition window.

A sensitivity analysis is performed on the various parameters affecting the performance of each image analysis algorithm.

The results obtained applying the image analysis techniques are compared to direct numerical simulations of turbulent flow in a channel obtained solving the unsteady Navier–Stokes equations at a Reynolds number of 3300 (based on the mean centreline velocity, U, and channel half-width, h) (Kim *et al* 1987). Figures 1 and 2 present mean velocity, turbulent intensities and Reynolds stress profiles normalized by the wall-shear velocity, u^*.

2. Data

Both experimental and numerical images presented in this contribution are matrices of 420 × 480 pixels with elements representing a light intensity $J(m, n)$ whose value ranges from 0 and 255. A continuous and differentiable function $I(x, y)$, collocated with the discrete function $J(m, n)$ at the grid points where pixels are located, is introduced.

2.1. Experimental images

Experiments were performed in a horizontal water channel of rectangular cross section (longitudinal dimension: 2.0 m) with a fully developed turbulent flow (figure 3). The channel cross

Table 1. Details of the experimental data.

Series	Re	U (cm s^{-1})	N_0	u^* (cm s^{-1})	d_{max} (cm)	Image number	PIV	FT	PTV	PN	PA (pixel^2)	MD (pixels)
1	2000	22.4	7.84	1.28	0.089	1536	×	×	–	1450	>22	7.6
2	2144	24.0	11.07	1.36	0.096	3584	×	×	–	1760	>18	6.6
3	2660	29.8	13.84	1.64	0.119	9216	×	×	–	1250	>21	7.8
4	2687	27.56	6.51	1.65	0.110	3584	–	×	–	760	>10	9.5
5	4850	54.3	4.60	2.77	0.217	10240	–	–	×			

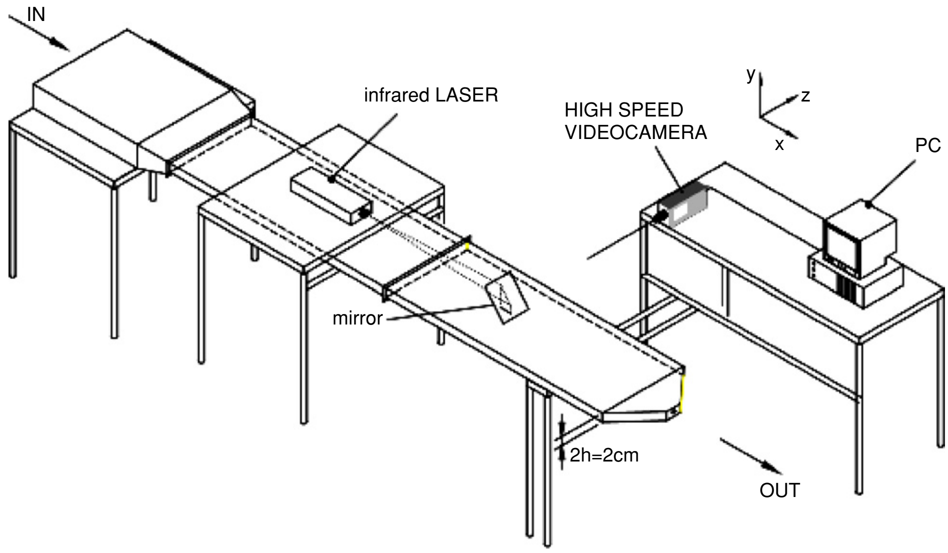

Figure 3. Experimental set-up (dimensions in cm).

section is 2 × 22 cm^2. Honeycombs and a 5:1 contraction upstream from the test section are employed. A water tank supplies the inlet of the channel. Different velocities are obtained by varying the height of the inlet vessel (Cenedese *et al* 1992). Measurements are made about 160 cm downstream of the inlet where the boundary layer is fully developed (Romano 1993). The water is collected into an outlet vessel and re-circulated. A Cartesian coordinate system is introduced where the x-axis is in the direction of flow, the y-axis is normal to the bottom of the channel, where the origin is located, and oriented positive upwards.

The infrared radiation of a laser diode array (maximum power equal to 15 W) is focused on a region of the x–y plane. The thickness of the laser sheet is about 1 mm. Images of tracers (pollen particles of 40 μm diameter and 1.06 g cm^{-3} density (Gullo *et al* 2002)) are recorded using a high-speed video camera. The particles are injected into the flow at a point located 130 cm from the acquisition window. The camera can acquire from 50 to 1000 frames per second (fps). The number of acquired images as well as their resolution depends on the frame rate. Images are stored directly in the memory of a computer. For the present set of measurements, the time interval between images, as well as the temporal resolution, is 1/250 s. The dimensions of the acquired area are 2 × 2.28 cm^2.

Table 1 shows the Reynolds number for each set of experiments, based on h (channel half-width) and U (centreline velocity). The three image analysis methods produce nearly identical values for U. The seeding concentration is (Gullo *et al* 2002)

$$N_0 = N_p(A_0/A),$$

where N_p is the number of particles within the whole image of area A and A_0 is the region of analysis. We have assumed $A_0 = \pi d_{max}^2$, where d_{max} is the maximum displacement frame by frame. Some characteristics of those images analysed through the FT algorithm are presented in table 1, as well. PN represents the mean number of tracer particles per frame. The particle area (PA, in pixel^2) represents the average dimension of tracer particles. The centroid's minimum distance (MD, in pixels) represents the average minimum distance among couples of tracer particles. It was computed picking up a particle, computing its centroid, finding the closest centroid and averaging their distance with the analogous quantities for the other centroids belonging to the image. To separate the foreground (particles) from the background, a threshold level for image intensity has been introduced. This threshold, equal to 100, was computed by building an image intensity histogram.

Figures 4(a)–(c) display the negatives of images belonging to the sets analysed using different algorithms. Figure 4(a) belongs to series 3. Having a medium-high seeding density, it has been analysed using both PIV and FT. There is almost no light reflection on both walls. Figure 4(b) belongs to series 4. It is a medium-low seeding density image analysed with the FT algorithm. In fact, its density is too low to achieve accurate results with PIV (the interrogation window would be too large to contain enough particles) and too large to apply the PTV algorithm (the number of ambiguously

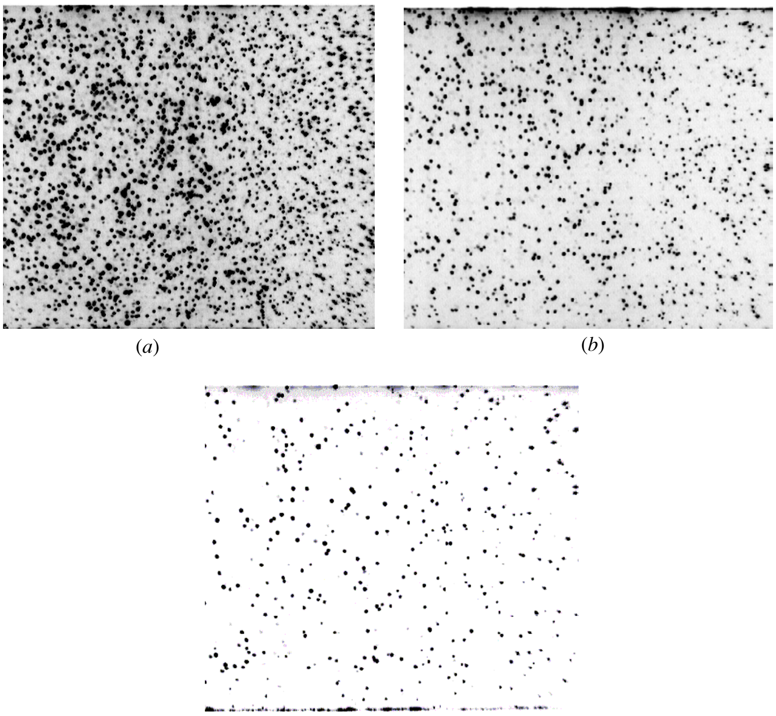

(*a*) (*b*)

(*c*)

Figure 4. Negatives of sample images belonging to series 3 (*a*), series 4 (*b*) and series 5 (*c*).

Table 2. Details of the synthetic data.

Series	*Re*	U (cm s^{-1})	N_0	u^* (cm s^{-1})	d_{max} (cm)	Image number	PIV	FT	PTV	PN	PA (pixel^2)	MD (pixels)
6	3300	36.96	7.084	1.98	0.141	2020	–	×	×	500	>21	11.2
7	3300	36.96	0.457	1.98	0.035	2005	–	×	×	500	>21	11.2

reconstructed trajectories increases with particle density). The upper part of the image presents light reflection. Figure 4(*c*) belongs to series 5. It is a low seeding density image analysed using the PTV algorithms. The average displacement of tracer particles is too large to be reconstructed with the FT algorithm. In fact, to keep processing time low, FT cannot track displacements larger than 1/10 of the image horizontal dimension. The image presents light reflection on both walls.

2.2. Synthetic images

The synthetic images generated follow traditionally accepted procedures (Cenedese *et al* 1993, Westerweel *et al* 1997, Fincham and Spedding 1997, Nogueira *et al* 1999, among others). The SIG (synthetic image generator) developed within EUROPIV2 is used (Moroni *et al* 2001). The flow field employed to generate the synthetic images corresponds to channel flow DNS data provided by the Laboratory for Aero and Hydrodynamics (AHD) of the Delft University of Technology (Haarlem 2000). Only one frozen frame of this DNS was used. The Taylor hypothesis allows advancing in time. The Reynolds number of this flow is $Re = 3300$.

Figure 5 presents a composition of ten synthetic images, each shifted with respect to the previous one along the streamwise direction of 24 pixels (about 0.8 times the mean axial velocity at the centre of the channel). The following features can be observed:

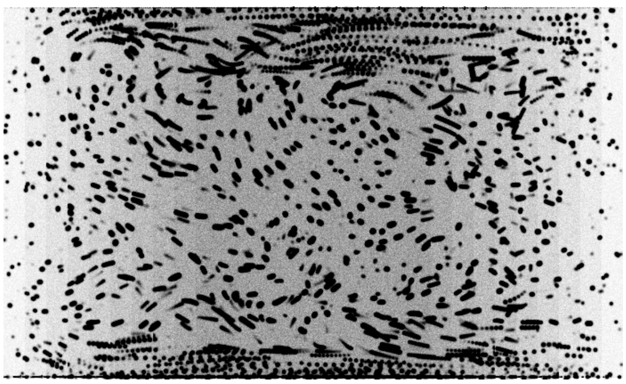

Figure 5. Composition of ten synthetic images subtracting 24 pixels between consecutive ones (series 7).

- there is no light reflection on the upper part of synthetic images;
- due to the light sheet homogeneity, in the synthetic images there is almost double the effective seeding density of the real images;
- the camera background noise in the synthetic images is random and not coherent as in real images.

The synthetic images of series 7 present mean displacements approximately 1/4 of those in series 6 (table 2). The synthetic images were analysed with both PTV and feature tracking.

3. Image analysis algorithms

3.1. Particle image velocimetry

Particle image velocimetry (PIV) is based on the comparison of two (or more) images of illuminated tracer particles which are assumed to be conservative. The displacement in time can be estimated by several methods, mainly using cross-correlation techniques, and the time separation between the images gives the velocity information for a subregion (interrogation area) of the whole imaged area.

Here we present the application of a standard PIV cross-correlation algorithm for image analysis (Cotroni *et al* 2000). The correlation error correction method proposed by Hart (1998) is implemented. When PIV is employed, errors are primarily due to lack of tracer particles or poor image quality and/or to correlation anomalies resulting from unmatched tracer images within the sample region. The method proposed by Hart allows both errors to be reduced by multiplying element by element each correlation table by the correlation table generated from the adjacent regions. The number of spurious determinations is reduced because any peak in one correlation table which does not exist within the other is smoothed. A recursive processing method which implements the window-offset technique (Westerweel 1997) is also introduced in the algorithm to reduce the size of the interrogation region and to increase the spatial resolution.

3.2. Particle tracking velocimetry

In contrast to PIV, in which the mean displacement of a small group of particles is sought, PTV tracks the path lines of individual particles. The main steps in PTV are (Udrea *et al* 2000)

- pre-processing the images to reduce background noise;
- determining tracer particle centroid coordinates in each frame with sub-pixel accuracy;
- tracking particle centroids frame by frame.

To track particles, a circle of fixed radius is centred on a particle centroid. A search is undertaken to find the same centroid at the next time within the circle. This effectively assumes a maximum velocity in the flow field. To add spots to the two-point trajectories, the nearest-neighbour principle ('minimum acceleration' criterion) within a circle of fixed radius is employed.

3.3. Feature tracking

Considering all surfaces inside the image to have Lambertian characteristics (their luminosity values do not depend on the point of view of the observer) and the illumination source to give almost constant light levels, the continuity equation for the so-called optical flow is obtained (Jahne 1997):

$$\frac{\mathrm{D}I}{\mathrm{D}t} = \frac{\partial I}{\partial t} + u\frac{\partial I}{\partial x} + v\frac{\partial I}{\partial y} = \frac{\partial I}{\partial t} + \nabla I^T \cdot \mathbf{U}$$
$$= I_t + uI_x + vI_y = 0, \tag{4}$$

where

$$\nabla I(\mathbf{x}, t) = \begin{bmatrix} \dfrac{\partial I(\mathbf{x}, t)}{\partial x} \\ \dfrac{\partial I(\mathbf{x}, t)}{\partial y} \end{bmatrix} = \begin{bmatrix} I_x \\ I_y \end{bmatrix}, \qquad \mathbf{U} = (u, v). \tag{5}$$

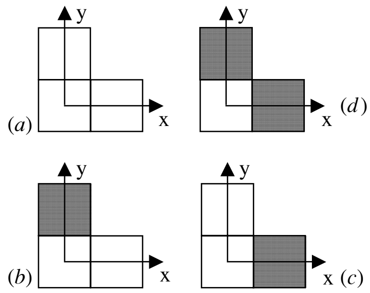

Figure 6. Intensity distribution along the x and y directions.

Equation (4) states that local variations in the intensity are balanced by convective changes. Sometimes, it is called the *image brightness constancy constraint* (BCC).

If equation (4) is computed at a single point, it only provides one equation for two unknowns, the velocity components. It is only when the equation is evaluated at each point in a region W surrounding the one under investigation, that it provides sufficient information on $\mathbf{U}$ (Nishio *et al* 2001). The problem has to be reformulated as a minimization in a least-squares sense and the solution will be a velocity vector that better approximates the motion of the interrogation window. In a purely translational motion model, the motion is assumed to be constant in the interrogation region ('frozen' hypothesis).

In the purely translational motion model, the line integral over the window centroid path can be represented as the difference between the values at the extremes of the path itself. A cost function SSD, sum of squared differences, over a window W surrounding the feature under investigation representing the dissimilarity between the image I at time t_A (I_A) and at successive time $t_\mathrm{B} = t_\mathrm{A} + \Delta t$ (I_B), can be written (Lucas and Kanade 1981, Tomasi and Kanade 1991). As

$$I_\mathrm{B} = I_\mathrm{A} + \left(\frac{\mathrm{D}I}{\mathrm{D}t}\right)_{t_\mathrm{A}} \Delta t,$$

we obtain

$$\mathrm{SSD} = \frac{1}{W\Delta t^2}\int_W \{I_\mathrm{B} - I_\mathrm{A}\}^2 \,\mathrm{d}S = \frac{1}{W}\int_W \left\{\left(\frac{\mathrm{D}I}{\mathrm{D}t}\right)_{t_\mathrm{A}}\right\}^2 \mathrm{d}S$$
$$= \frac{1}{W}\int_W \left\{\left(\frac{\partial I}{\partial t} + \nabla I^T \cdot \mathbf{U}\right)\right\}^2 \mathrm{d}S. \tag{6}$$

This is a quadratic function of the velocity $\mathbf{U}$. As a consequence, the minimization problem can be solved in a closed form (Tomasi and Kanade 1991).

To obtain a least-squares estimation of $\mathbf{U}(\mathbf{x})$, the derivative of the cost function SSD with respect to $\mathbf{U}$ is evaluated:

$$\frac{\partial\,\mathrm{SSD}}{\partial \mathbf{U}} = \frac{2}{W}\int_W \nabla I \left(\nabla I^T \cdot \mathbf{U} + \frac{\partial I}{\partial t}\right) \mathrm{d}S$$
$$= 2\int_W \left\{\begin{bmatrix} I_x^2 & I_x I_y \\ I_y I_x & I_y^2 \end{bmatrix} \cdot \mathbf{U} + \begin{bmatrix} I_x I_t \\ I_y I_t \end{bmatrix}\right\} \mathrm{d}S. \tag{7}$$

Setting (7) to zero,

$$\begin{bmatrix} \displaystyle\int_W I_x^2 \,\mathrm{d}S & \displaystyle\int_W I_x I_y \,\mathrm{d}S \\ \displaystyle\int_W I_y I_x \,\mathrm{d}S & \displaystyle\int_W I_y^2 \,\mathrm{d}S \end{bmatrix} \cdot \mathbf{U} + \begin{bmatrix} \displaystyle\int_W I_x I_t \,\mathrm{d}S \\ \displaystyle\int_W I_y I_t \,\mathrm{d}S \end{bmatrix} = 0,$$

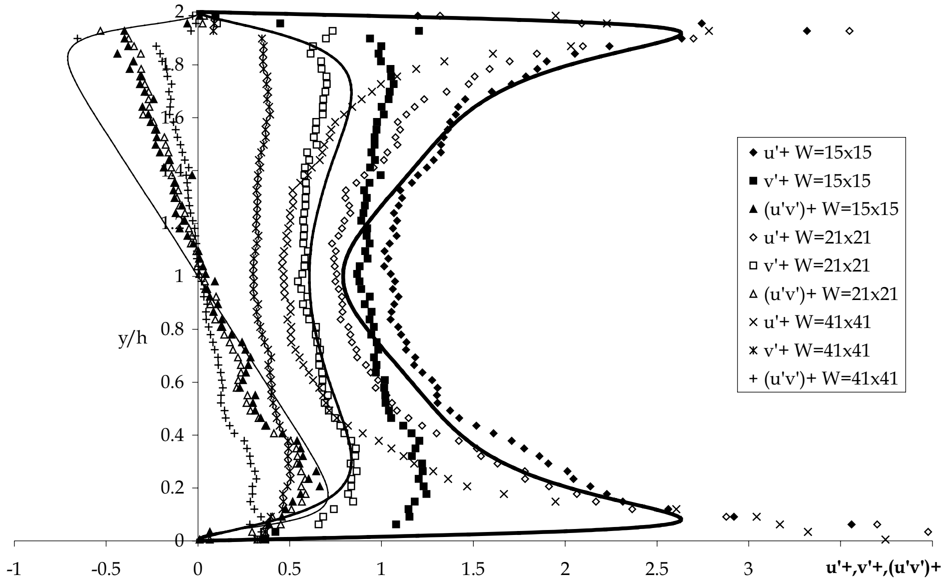

Figure 7. FT algorithm. Turbulent intensities and Reynolds stresses normalized by the wall-shear velocity (series 7): effect of window size.

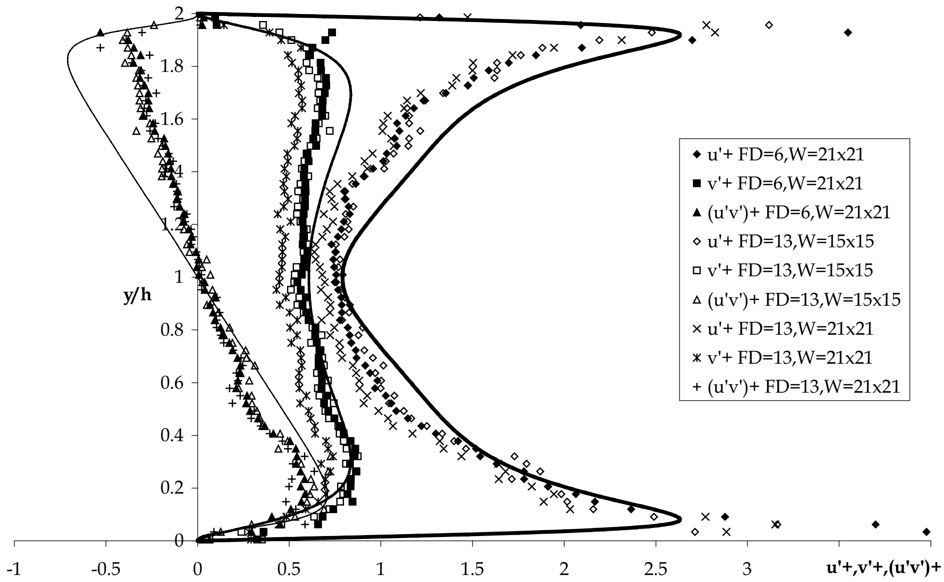

Figure 8. FT algorithm. Turbulent intensities and Reynolds stresses normalized by the wall-shear velocity (series 7): effect of minimum feature distance.

or more simply,

$$\underline{\mathbf{G}} \cdot \mathbf{U} + \mathbf{b} = 0, \qquad \mathbf{U} = -\underline{\mathbf{G}}^{-1} \cdot \mathbf{b}. \tag{8}$$

The square matrix $\underline{\mathbf{G}}$ is invertible if both eigenvalues λ_1 and λ_2 are non-zero. Three different cases are possible:

- $I_x = 0$ and $I_y = 0$, i.e. uniform intensity distribution in both directions (figure 6(*a*)): both eigenvalues are zero ($\lambda_1 = \lambda_2 = 0$);
- $I_x = 0$ and $I_y \neq 0$, i.e. uniform intensity distribution in the *x* direction (figure 6(*b*)), or $I_x \neq 0$ and $I_y = 0$, i.e. uniform intensity distribution in the *y* direction (figure 6(*c*)): one eigenvalue is null ($\lambda_1 > 0$; $\lambda_2 = 0$);
- $I_x \neq 0$ and $I_y \neq 0$, i.e. nonuniform intensity distribution in both directions (figure 6(*d*)): both eigenvalues are positive ($\lambda_1 \rangle 0$; $\lambda_2 \rangle 0$).

It is important to note that the existence of a solution for the system in (8) depends only on the invertibility of the matrix $\underline{\mathbf{G}}$. This means that it is possible to create an algorithm that is capable of analysing when and with what accuracy the velocity **U** can be estimated by computing spatial derivatives of the image luminosity: in other words, the FT algorithm defines implicitly the features that are good to track.

3.4. Validation criteria

Particle flow is coherent motion, in which spatially close particles are likely to have similar displacement vectors. To enhance trajectory accuracy and, as a consequence, velocity estimation, coherence-based in-line processing can

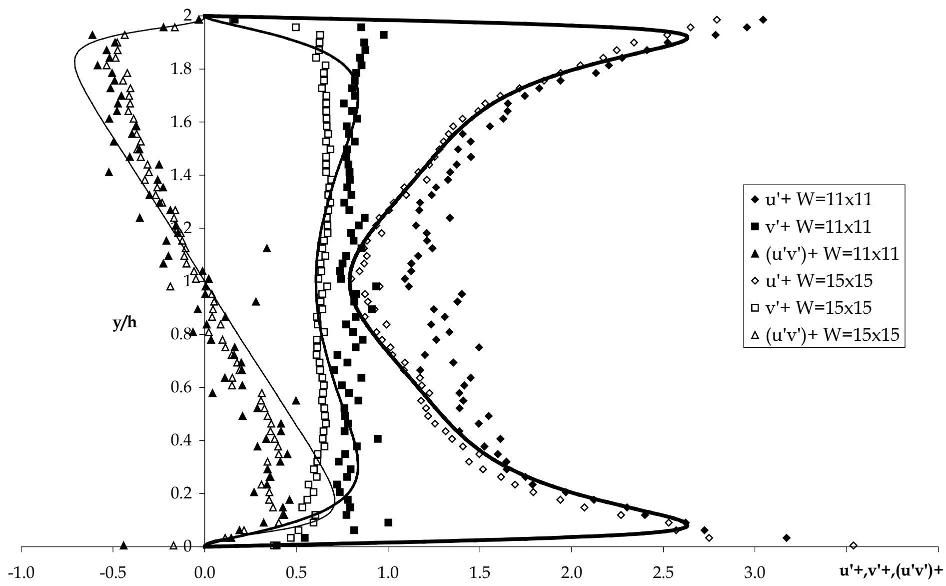

Figure 9. FT algorithm. Turbulent intensities and Reynolds stresses normalized by the wall-shear velocity (series 1): effect of window size.

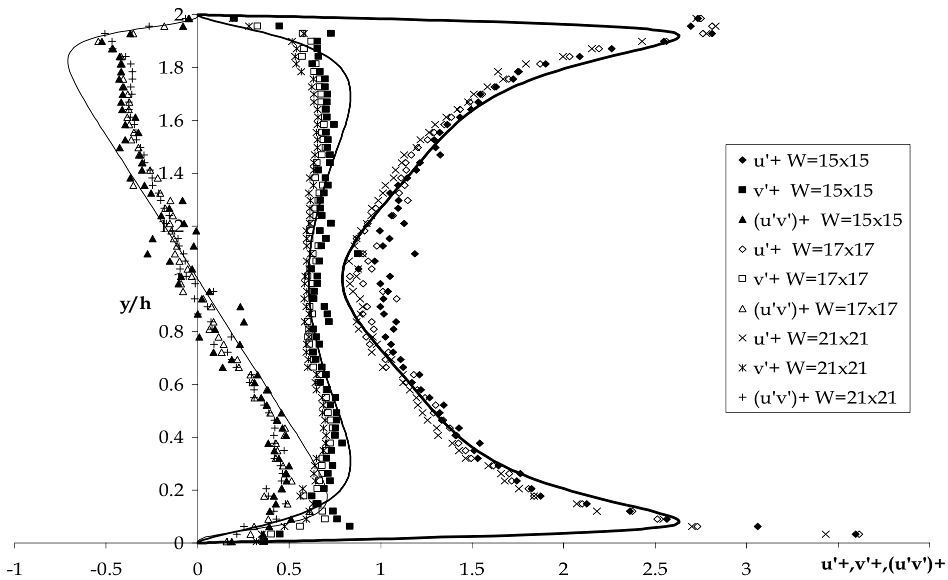

Figure 10. FT algorithm. Turbulent intensities and Reynolds stresses normalized by the wall-shear velocity (series 2): effect of window size.

be applied to the 'raw' displacement field (Verestoy *et al* 1999). Coherence filtering eliminates velocity vectors if they are incompatible with the dominant surrounding vectors.

3.4.1. PIV algorithm. Each data set obtained by the application of the PIV algorithm is subjected to a validation procedure suitable for detecting and replacing spurious displacements. Two validation criteria have been simultaneously implemented:

- a local median-filtering method (Westerweel 1994) to identify displacement vectors that deviate by more than a given amount in magnitude (20%) or direction (20%) from adjacent vectors;
- a peak-height validation where the highest peak is compared with the second highest one and validated if the ratio is greater than a predefined value ($\delta = 1.2$) (Keane and Adrian 1992).

Different flags are associated with the spurious vectors detected from each of the previous two validation criteria in order to employ this information in the following statistical analysis as a rejection criterion.

3.4.2. Tracking algorithms: the coherence filter. A median-filtering procedure (Rousseeuw and Leroy 1987) has been implemented within the FT algorithm for detecting spurious vectors. Given a feature point and its velocity, we looked at a minimum number (7) of points lying around that feature. The vector magnitude is compared to the median value to check if it deviates less than 20%.

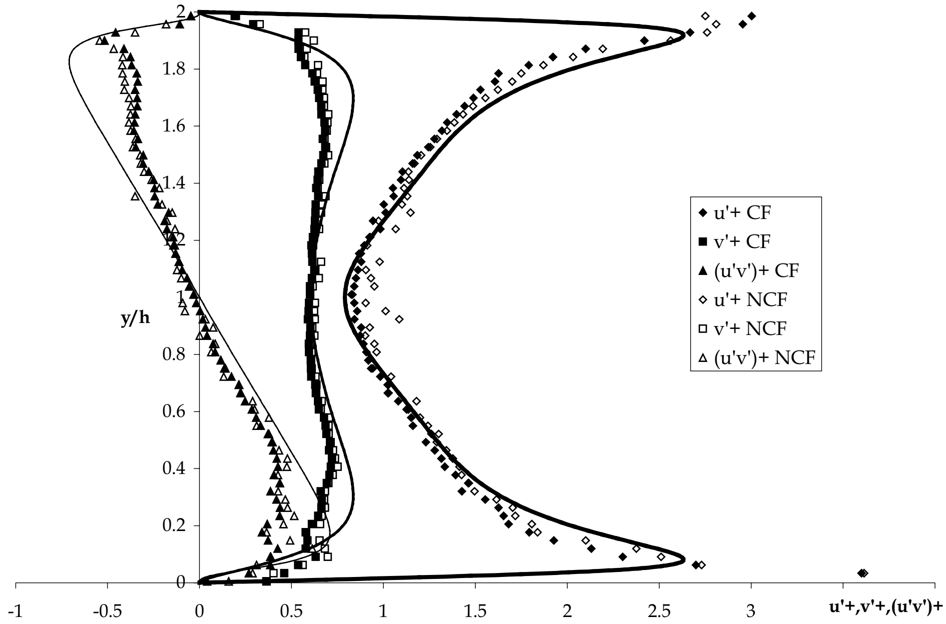

Figure 11. FT algorithm. Turbulent intensities and Reynolds stresses normalized by the wall-shear velocity (series 2): effect of the coherence filter (CF: coherence filter applied; NCF: coherence filter not applied).

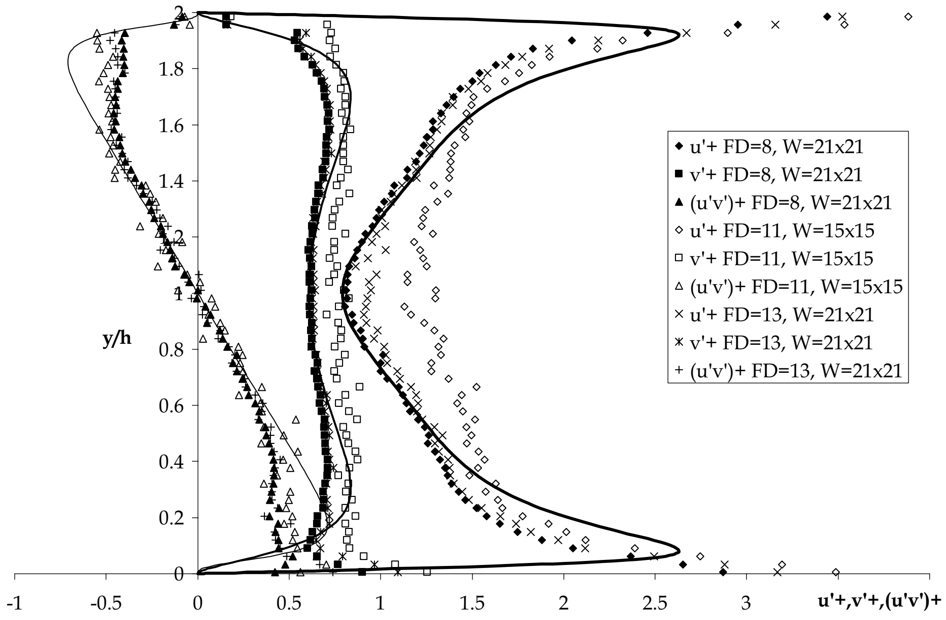

Figure 12. FT algorithm. Turbulent intensities and Reynolds stresses normalized by the wall-shear velocity (series 3): effect of minimum distance and window size.

If the condition is not satisfied, the vector can be either discharged (and the tracking of the feature interrupted) or substituted with the median value of the cluster.

Due to the low particle density, velocity vectors computed from trajectories reconstructed by means of the PTV algorithm with at least three spots are considered validated.

4. Results

Turbulent flows are significantly affected by the presence of walls. Both the mean and the fluctuating velocity are affected by the no-slip boundary condition. The turbulence is also changed by the presence of the wall. Close to the wall, viscous damping reduces the tangential velocity fluctuations, while kinematic blocking reduces the normal fluctuations. In the outer part of the near-wall region, there is a significant production of turbulent kinetic energy due to the large gradients in mean velocity.

The near-wall region can be subdivided into three layers. In the innermost layer, called the viscous sublayer, the (molecular) viscosity plays a dominant role in momentum and heat or mass transfer. In the outer layer, called the fully

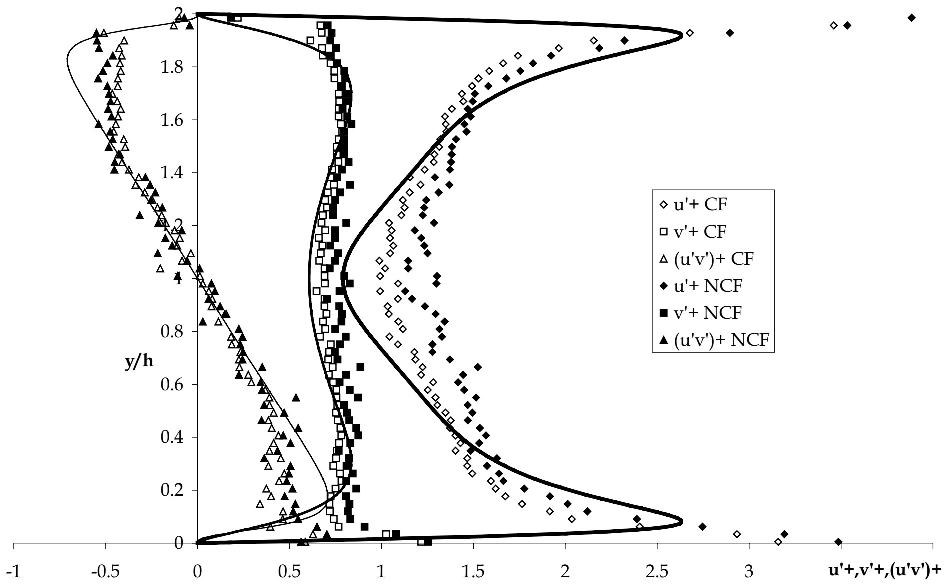

Figure 13. FT algorithm. Turbulent intensities and Reynolds stresses normalized by the wall-shear velocity (series 3): effect of the coherence filter (CF: coherence filter applied; NCF: coherence filter not applied).

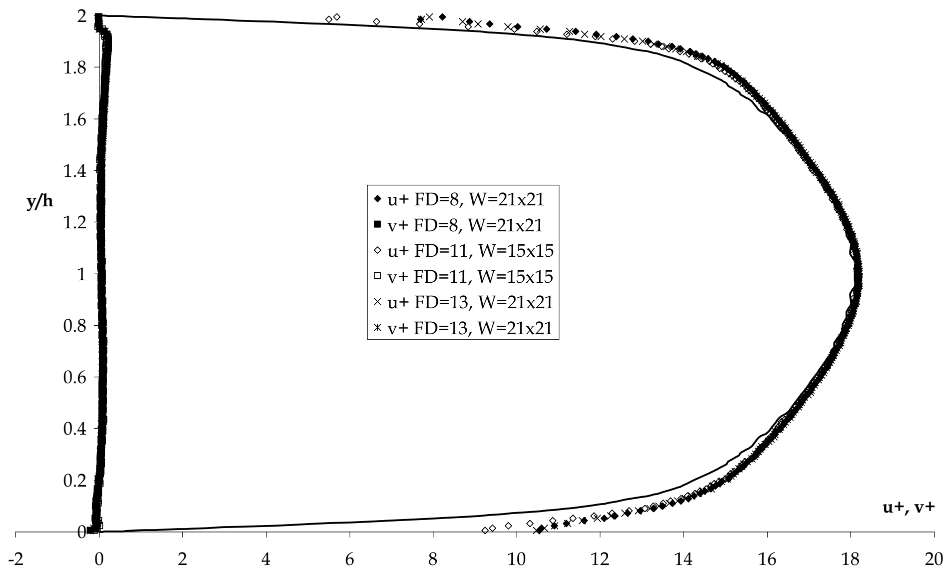

Figure 14. FT algorithm. Mean velocity profiles normalized by the wall-shear velocity (series 3).

turbulent layer, Reynolds stresses play a major role. In the intermediate region between the viscous sublayer and the fully turbulent layer, both molecular viscosity and Reynolds stresses are important.

All figures reported below present the comparison among mean velocity, turbulent intensities for both velocity components and Reynolds stress profiles computed from synthetic and experimental data and the DNS results from Kim *et al* (1987), represented as continuous lines. The similarity of our data to DNS profiles is the measure of the image analysis algorithm quality and performance.

4.1. FT results

To test the feature tracking algorithm and coherence filter (if applied) performances, the following parameters have to be taken into account:

- FD: minimum distance among features. This must be chosen according to image seeding density. This parameter has a completely different role than the parameters input into the PTV algorithm. It has no effect on the trajectories reconstructed, but only determines the quantity of features to track and, as a consequence, the number and density of the velocity vectors.
- LMIN: threshold on the second eigenvalue. This is introduced to take into account the noise inside the image and has an influence on feature density. Its choice is less critical than FD. For this reason, it has been kept constant.
- $\sqrt{W}$: window side size (square windows). This parameter influences tracking efficiency.

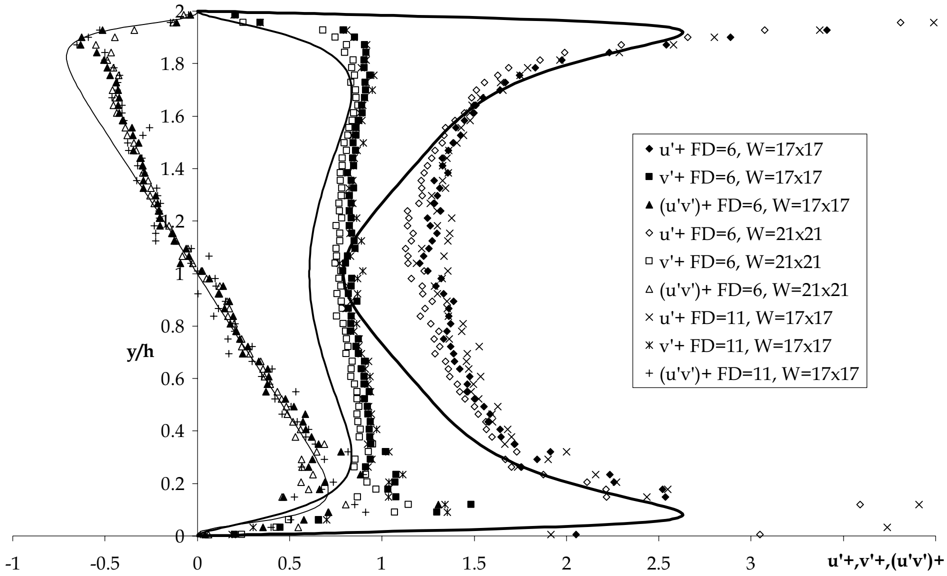

Figure 15. FT algorithm. Turbulent intensities and Reynolds shear stresses normalized by the wall-shear velocity (series 4): effect of window size and minimum feature distance.

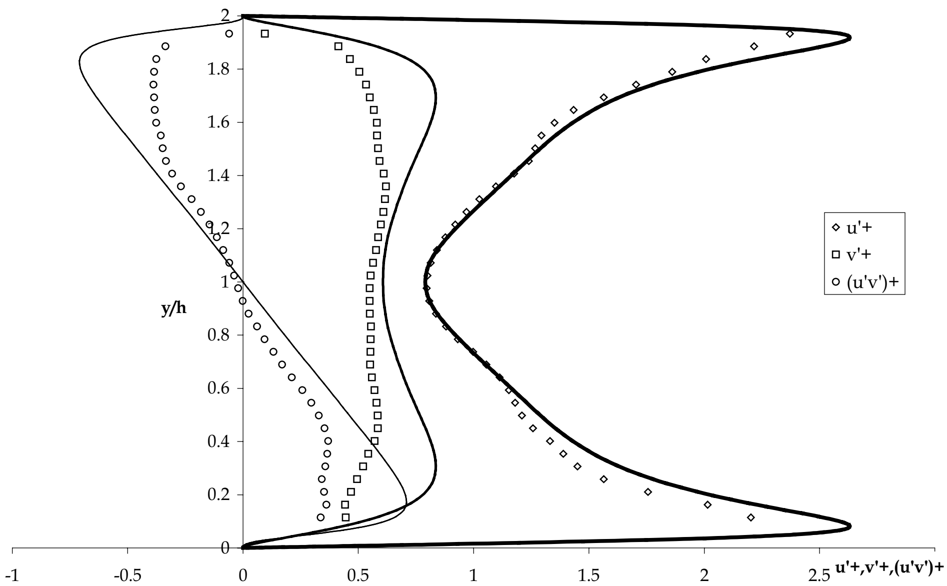

Figure 16. PIV algorithm. Turbulent intensities and Reynolds stresses normalized by the wall-shear velocity (series 1).

- CF: application of the coherence filter to validate feature velocity. This may have a large influence on final results. Tracking of features deviating from the median value more than 20% is always interrupted.

Particle tracking procedures, FT as well as PTV, yield a number of trajectories from which two velocity components can be computed. The Gaussian method has been used to interpolate these data onto a regular grid. In this regard, SSD values, representing the errors associated with the velocity vectors reconstructed, have been output together with feature positions and velocity components to be used to validate the vector components during this resampling procedure. In fact, each set of data has a mean error (μ_{SSD}) and a variance $\left(\sigma^2_{\mathrm{SSD}}\right)$ associated with it. The velocity components taken into account within the resampling procedure were the ones with error (SSD), satisfying the condition SSD $\leqslant \mu_{\mathrm{SSD}} + \sigma_{\mathrm{SSD}}$. Furthermore, assuming homogeneity in thin horizontal slices, profiles of the quantities of interest were computed by averaging over slices in both time and space (along x). The thickness of these slices is about 2 pixels (about 0.095 mm) giving a total of 210 slices. The number of samples belonging to each slice is in each case adequate to have reliable statistics (more than 1000 samples). To present more readable profiles, data are undersampled by a factor of 3, providing a final number of slices equal to 70.

Table 3 presents, for each figure reported herein

- the parameters input into the FT algorithm;
- the resolution achieved (the point coordinate closest to the

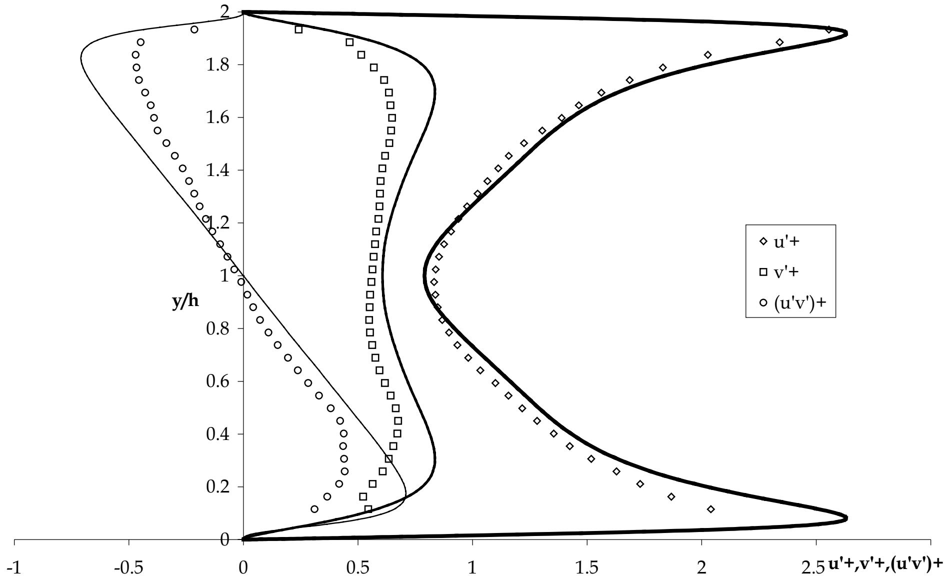

Figure 17. PIV algorithm. Turbulent intensities and Reynolds stresses normalized by the wall-shear velocity (series 2).

Table 3. Image analysis parameters and performance for FT.

Figure	Series	FD (pixels)	$\sqrt{W}$ (pixels)	CF	Resolution (cm)	$\varepsilon_{u'+}$	$\varepsilon_{v'+}$	$\varepsilon_{(u'v')+}$	FN
7	7	6	15	No	0.014	0.188	0.324	0.179	2650
7	7	6	21	No	0.014	0.230	0.100	0.194	3100
7	7	6	41	No	0.043	0.577	0.335	0.307	3040
8	7	6	21	No	0.014	0.230	0.100	0.194	3100
8	7	13	15	No	0.014	0.239	0.095	0.168	440
8	7	13	21	No	0.043	0.302	0.176	0.200	460
9	1	9	11	No	0.062	0.242	0.177	0.181	1410
9	1	9	15	No	0.043	0.102	0.123	0.168	1060
10	2	13	15	No	0.043	0.151	0.118	0.153	622
10	2	13	17	No	0.043	0.131	0.097	0.146	637
10	2	13	21	No	0.043	0.145	0.116	0.161	641
11	2	13	17	Yes	0.062	0.151	0.106	0.173	581
11	2	13	17	No	0.043	0.131	0.097	0.146	637
12	3	8	21	No	0.062	0.236	0.090	0.141	1230
12	3	11	15	No	0.062	0.273	0.140	0.113	650
12	3	13	21	No	0.062	0.209	0.095	0.135	620
13	3	11	15	Yes	0.062	0.236	0.090	0.143	975
14	3	11	15	No	0.062	0.273	0.140	0.113	650
15	4	11	17	Yes	0.100	0.325	0.192	0.113	530
15	4	6	21	Yes	0.072	0.234	0.125	0.104	1320
15	4	6	17	Yes	0.100	0.300	0.185	0.101	1150

wall where the accuracy is acceptable, defined as the first point starting from the wall where the difference between experimental and numerical results is less than 20%, neglecting the case of accuracy getting worse moving towards the centreline). When the resolutions for the upper and the lower wall are different, the smaller value is considered;

- a set of three numbers $\varepsilon_{u'+}$, $\varepsilon_{v'+}$, $\varepsilon_{(u'v')+}$ describing the accuracy of turbulence intensity in the streamwise direction ($\varepsilon_{u'+}$), turbulence intensity in the normal direction ($\varepsilon_{v'+}$) and Reynolds stresses ($\varepsilon_{(u'v')+}$). Those quantities, square roots of squared differences between experimental results and DNS results from Kim *et al* (1987) ($\widetilde{u}'+$, $\widetilde{v}'+$ and $(\widetilde{(u'v')}+)$)

$$\varepsilon_{u'+} = \sqrt{\sum ((u'+) - \widetilde{u}'+)^2/N}, \qquad (9)$$

$$\varepsilon_{v'+} = \sqrt{\sum ((v'+) - \widetilde{v}'+)^2/N}, \qquad (10)$$

$$\varepsilon_{(u'v')+} = \sqrt{\sum (((u'v')+) - (\widetilde{u'v'})+)^2/N} \qquad (11)$$

are computed considering the portion of the vertical profile within the limits identified by the resolution achieved;

- the average number of features (FN) tracked by the algorithm. The average number of velocity vectors per series is the product of FN and the image number.

4.1.1. Results on synthetic images. Figure 7 presents turbulent intensities for both velocity components and

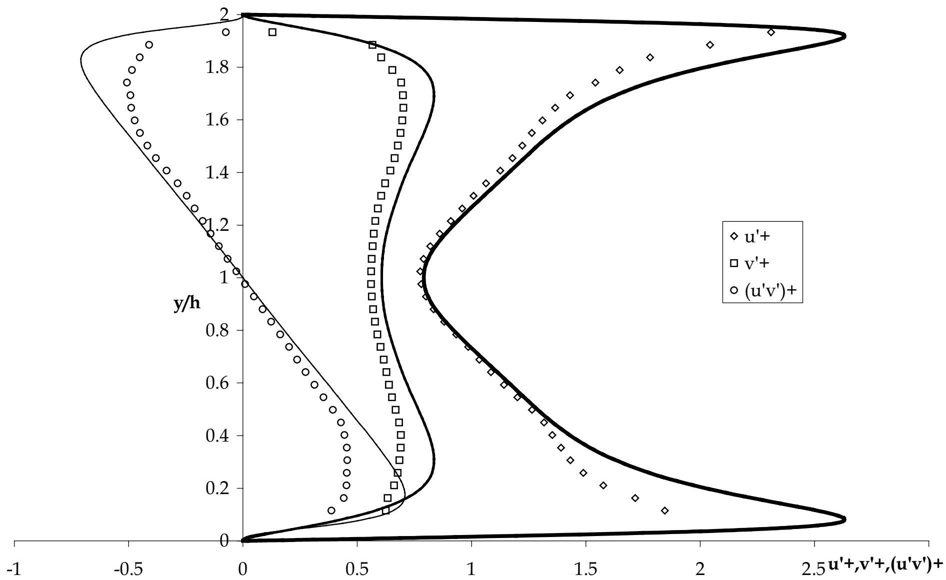

Figure 18. PIV algorithm. Turbulent intensities and Reynolds stresses normalized by the wall-shear velocity (series 3).

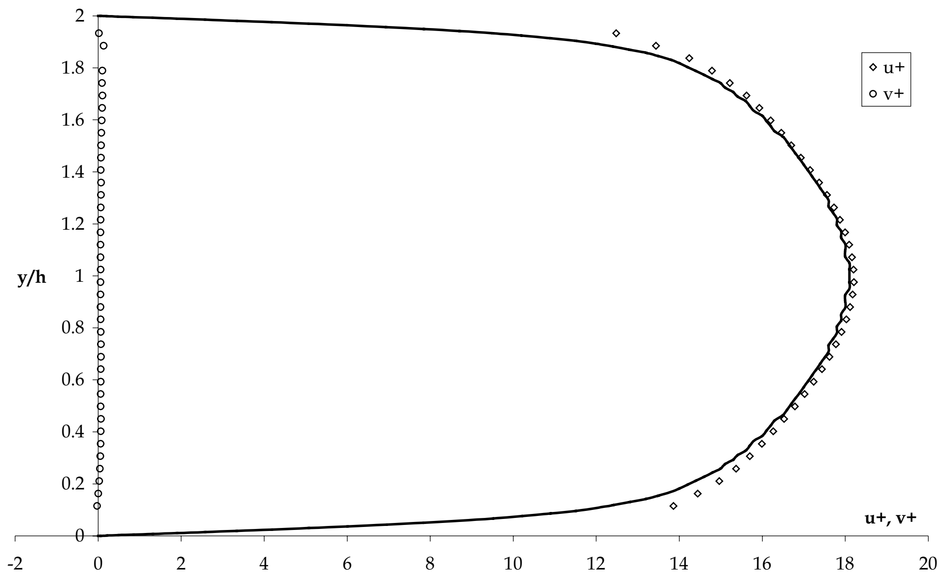

Figure 19. PIV algorithm. Mean velocity profile normalized by the wall-shear velocity (series 3).

Reynolds stresses for data in series 7. The seeding density is the lowest available. The effect of window size is tested and the minimum distance among features is constant at 6 pixels (about 0.3 mm). When the separation among features is small, the result becomes very sensitive to the size of W. Large windows are associated with larger errors. The best results in terms of matching our profiles and those obtained by DNS (except the turbulent intensity in the y direction, see table 3) are achieved when the window dimension is set to 15 pixels (about 0.71 mm). For these dimensions, the number of features successfully tracked is lower than for the other two cases but always large compared to the number of tracer particles within the images (about 500). When the distance among features is lower than the average minimum distance among centroids and/or the average particle diameter, the same particle will have more than one feature associated with it. If this occurs, the same particle will be tracked a number of times, overconditioning the resulting statistics.

Figure 8 presents turbulent intensities for both velocity components and Reynolds stresses for data in series 7 with the aim of testing the effect of increasing the minimum feature distance and, as a consequence, decreasing the number of features tracked. The 'best result' in terms of matching of experimental and numerical profiles and resolution is achieved for FD = 13 pixels (about 0.62 mm) and $W = 15 \times 15$ pixels (0.71×0.71 mm^2) (see table 3). In this case, the number of features tracked is very close to the number of particles seeding the fluid. Small windows are always associated with smaller errors. It should also be noted that to account for the camera thermal noise, synthetic images have been generated adding a random value from 0 to 16 pixels to the grey level. The

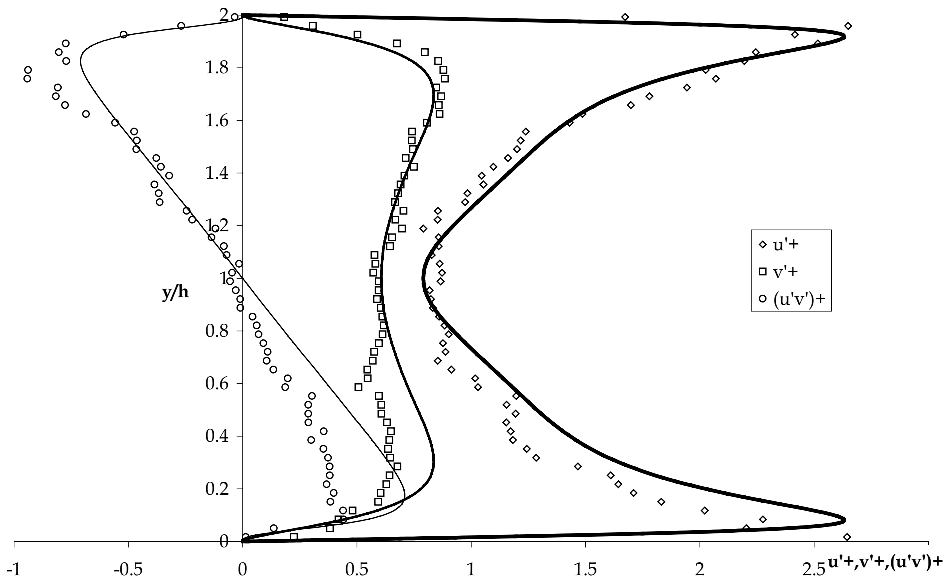

Figure 20. PTV algorithm. Turbulent intensities as a function of depth for series 7.

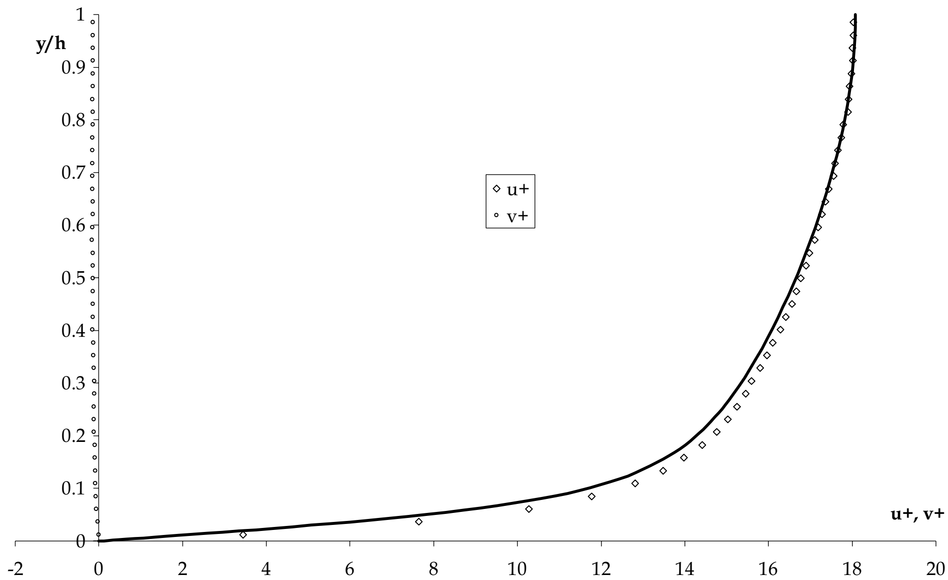

Figure 21. PTV algorithm. Plot of the mean velocity as a function of depth (series 5).

effect of this incoherent noise is lower accuracy of velocity vectors reconstructed using large windows, which have a large percentage of background around the features under investigation.

4.1.2. Results on experimental images. Figure 9 presents turbulence intensities and Reynolds stresses of the streamwise and normal velocity components for series 1. The effect of feature window width and height is investigated. The feature distance is set to 9 pixels (about 0.43 mm). The window sizes range from 11 × 11 pixels (0.52 × 0.52 mm^2) to 15 × 15 pixels (0.71 × 0.71 mm^2). Small windows lead to large oscillations in the final profiles and worse matching with reference profiles (table 3). Since the image noise is coherent, the accuracy of velocity vectors is larger for large windows than for small windows. Also, the resolution is larger (first accurate point closer to the wall) for larger windows.

Figure 10 presents the same kind of comparison for series 2. Window sizes range from 15 × 15 pixels (0.71 × 0.71 mm^2) to 21 × 21 pixels (1.00 × 1.00 mm^2). The match with Kim *et al*'s (1987) results is rather good for each window size.

Figure 11 presents the effect of the coherence filter for series 2. The window height and width are set to 17 pixels while the minimum distance among features is set to 13 pixels (about 0.62 mm). The coherence filter does not significantly affect the velocity field. However, by eliminating outliers among displacements, it does make the profile smoother.

Figures 12 and 13 present results for series 3. In this case, a 21 × 21 pixel window and FD = 8 produce the

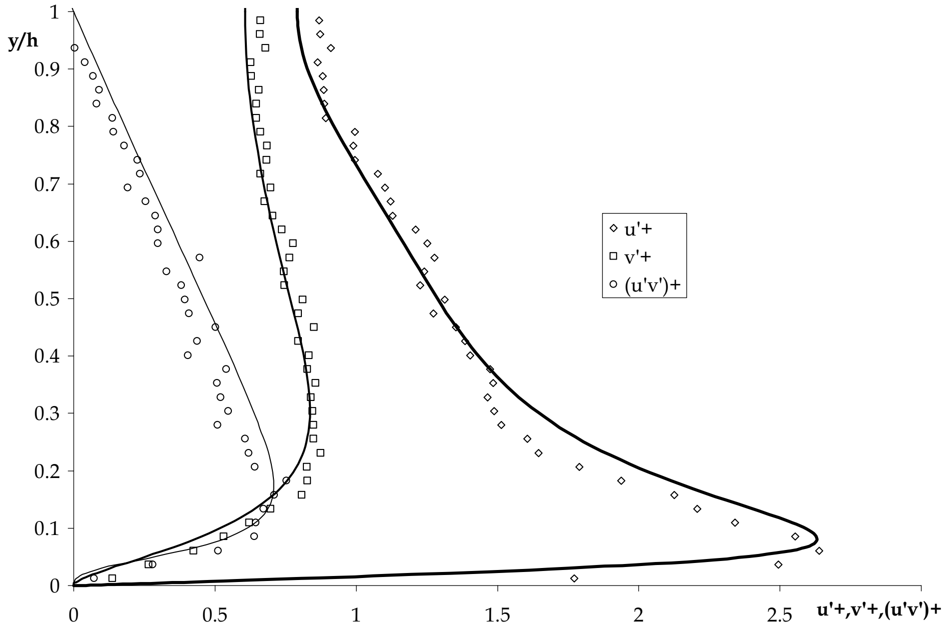

Figure 22. PTV algorithm. Plot of the velocity variance as a function of depth (series 5).

best matches with Kim *et al*'s (1987) data (table 3). The number of features tracked is also very close to the number of tracer particles. The coherence filter slightly modifies the quantities under investigation (see figure 13). This is particularly true for the turbulent intensities of the axial velocity component. Coherence prevents the overestimation of displacement vectors.

Figure 14 presents the mean velocity profiles for series 3, with the aim of determining their dependence on feature distance and window sizes. Figure 14 is reported as an example of general behaviour, with the profiles collapsing on one another. The match with the DNS results is very good in the area around the centreline but the results get worse close to the wall. The same result is obtained for each series. All plots showing the profiles computed from FT data have very low quality data near the walls because of their coincidence with the boundary of the image. It is not possible to build windows around features belonging to regions close to walls. The code tracks those features however, but their accuracy will be much lower than the accuracy at the other points. A larger acquisition window might allow wall data to be tracked with the same accuracy as that in the channel. The acquisition window was chosen so that the spatial resolution is the largest possible.

The applicability of feature tracking algorithms is not dependent on seeding density. Figure 15 corresponds to the FT algorithm applied to series 4. The coherence filter has to be applied to avoid a large number of spurious displacement vectors. The number of incorrect displacement vectors largely increases when the seeding density decreases. The turbulent intensities of both velocity components are slightly overestimated. The Reynolds stress profile nicely collapses onto the profile of Kim *et al* (1987). The parameters for image analysis (both window size and minimum feature distance) do not significantly affect the results.

4.2. PIV results

Due to the low particle density within synthetic images available at this stage, the application of PIV algorithms is not recommended. The subsequent results apply to PIV with high particle density.

4.2.1. Results on experimental images. Figures 16–18 display profiles of turbulence intensities and Reynolds stresses for the axial and normal components of velocity for series 1–3. The mean velocity for the axial and normal components of velocity for series 3 is reported as well (figure 19). The parameters for the PIV analysis are as follows: 32×32 window size, overlapping equal to 70%, window offset, three levels of analysis in the multi-grid approach and sub-pixel Gaussian. The correlation error correction method was not employed. The flags associated with spurious vectors were used as rejection criteria in the statistical analysis. Spurious vectors represent less than 5% of the total number. They are mainly located along the exit cross section. Profiles are plotted against height which is normalized by the channel half-width.

The results obtained from PIV are smoothed in space in comparison to those derived from other velocity measurement techniques. This is a result of the finite correlation-window size.

4.3. PTV results

4.3.1. Results on synthetic images. Figure 20 displays turbulent intensities and Reynolds stresses as a function of depth for series 7.

By decreasing the time lags between frames (series 6 presents a time lag four times larger than series 7), we find that both turbulent intensities and Reynolds stresses are closer to Kim *et al*'s (1987) results. The small number of samples available for computing statistics gives rise to data scatter. More details on the application of the PTV algorithm to series 6 and series 7 and the way it compares to feature tracking results can be found in Moroni *et al* (2004).

4.3.2. Results on experimental images. Figure 21 shows the mean velocity profiles as a function of depth for series 5 (Gullo *et al* 2002). Figure 22 displays turbulent intensities and Reynolds stresses as a function of depth. Experimental profiles are compared to DNS data (Kim *et al* 1987). To increase the spatial resolution, only half of the channel was investigated. The experimental mean velocity agrees with DNS results. We emphasize here that an improved match among experimental curves and DNS profiles can be obtained by increasing the friction velocity. We do so in the data of series 5 with the intent of emphasizing the difficulties in determining the 'right' friction velocity from empirical formulae.

There is a good agreement among turbulent intensities and Reynolds stresses between the experiments and DNS data. Statistics are adequate in each figure (more than 1000 samples per layer).

Data from series 5 present a large $d_{\max}$ (0.217 cm) and for this reason are not suitable to be analysed with our feature tracking algorithm.

5. Conclusions

Optical flow seems a very promising technique capable of accurately reconstructing the velocity field even when large gradients occur. Since there are no constraints on particle density, running experiments becomes much easier. However, the algorithm performs better when applied to high particle density images. The number of samples can be set very high with the appropriate choice of the minimum feature distance and threshold on the second eigenvalue of the light intensity gradient matrix. The possibility of outputting the SSD associated with the feature allows one to undersample the set of data resulting from applying the algorithm and extracting only the most accurate velocity vectors. The parameters input into the method may have an influence on the results, but they have a different meaning than those on which classical PTV algorithms are based. Feature density and accuracy of the velocity vectors are functions of those parameters but their choice depends on image characteristics and not on flow peculiarities. On the other hand, the application of PIV algorithms requires the input of window size and overlapping, conditioning the achieved resolution.

Furthermore, even if this paper is focused on computing Eulerian quantities, FT is a Lagrangian technique allowing the reconstruction of tracer particle trajectories. Cenedese *et al* (2004a, 2004b, 2004c) present some Lagrangian results from the application of FT.

Table 4 shows a schematic representation of the result quality for data under investigation. This table shows that results are comparable for all techniques, as well as for the achieved resolution. The paper is focused on testing the FT algorithms. More details on PIV and PTV analyses can be found in Moroni *et al* (2001) and Cenedese *et al* (2002).

The increase in accuracy of trajectories of features close to the border must still be taken into account. Furthermore, the implementation of the affine model would improve the accuracy of the results mainly where the velocity field presents large gradients. The affine methods would also allow translation, rotation, scale and shear of the interrogation window, providing refined velocity gradients and displacement vectors as final results when compared to those provided by the application of the translational motion model (Miozzi 2004).

Table 4. Accuracy of the results for PIV and PTV.

Figure	Series	Technique	Resolution (cm)	$\varepsilon_{u'+}$	$\varepsilon_{v'+}$	$\varepsilon_{(u'v')+}$
16	1	PIV	0.067	0.119	0.189	0.195
17	2	PIV	0.067	0.130	0.132	0.156
18	3	PIV	0.067	0.216	0.097	0.136
20	7	PTV	0.050	0.183	0.102	0.156
22	5	PTV	0.061	0.102	0.043	0.068

Acknowledgments

This work has been partially performed under the EUROPIV2 and PIVNET2 projects. The authors would like to thank Professor José Nogueira for generating the synthetic images (series 6 and 7) and Professor Romano for useful suggestions and discussion about the topics covered in this paper and for providing the data of series 5. Thanks are also given to Jason Hyatt of the Woods Hole Oceanographic Institution for assistance in improving the English.

References

Adrian R J 1991 Particle imaging techniques for experimental fluid mechanics *Ann. Rev. Fluid Mech.* **23** 261–304

Cenedese A, Costantini A and Romano G P 1992 LDA spectral measurements in a turbulent boundary layer *Exp. Therm. Fluid Sci.* **5** 281–9

Cenedese A, Del Prete Z, Miozzi M and Querzoli G 2004a A laboratory model of the left ventricle of human heart *Proc. 12th Int. Symp. on Application of Laser Techniques to Fluid Mechanics (Lisbon)*

Cenedese A, Espa S and Miozzi M 2004b Experimental study of two-dimensional turbulence using feature tracking *Proc. 12th Int. Symp. on Application of Laser Techniques to Fluid Mechanics (Lisbon)*

Cenedese A, Gullo G, Moroni M and Romano G P 2002 Lagrangian statistics in near-wall turbulence *Second Year Annual Report Within the European Project EUROPIV 2: A Joint Program to Improve PIV Performance for Industry and Research* Contract no G4RD-CT-2000-00190

Cenedese A, Miozzi M and Moroni M 2004c Penetrative convection in stratified fluids: velocity measurements by image analysis techniques *Proc. 12th Int. Symp. on Application of Laser Techniques to Fluid Mechanics (Lisbon)*

Cenedese A, Monti P and Sallustri M 1993 PIV: a numerical simulation *Proc. 5th Int. Conf. on Laser Anemometry Advances and Applications (Koningshof, 23–27 Aug.)*

Cenedese A, Moroni M and Viotti P 1997 Velocity field in a porous medium by means of stereoscopic particle image velocimetry *Proc. 7th Int. Conf. on Laser Anemometry Advances and Applications (Karlsruhe, 8–12 Sept.)*

Cenedese A and Querzoli G 1997 Lagrangian statistics and transilient matrix measurements by PTV in a convective boundary layer *Meas. Sci. Technol.* **8** 1553–61

Cenedese A, Romano G P and Antonia R A 1998 A comment on the 'linear' law of the wall for fully developed turbulent channel flow *Exp. Fluids* **25** 165–70

Cotroni A, Di Felice F, Romano G P and Elefante M 2000 Propeller tip vortex analysis by means of PIV *Exp. Fluids* **29** 227–36

Di Florio D, Di Felice F and Romano G P 2002 Windowing, re-shaping and re-orientation interrogation windows in particle image velocimetry for the investigation of shear flows *Meas. Sci. Technol.* **13** 953–62

Djenidi L, Dubief Y and Antonia R A 1997 Advantages of using a power law in a low $R\theta$ turbulent boundary layer *Exp. Fluids* **22** 348–50

Fincham A M and Spedding G R 1997 Low-cost, high resolution DPIV for measurement in turbulent fluid flows *Exp. Fluids* **23** 449–62

Gullo G, Querzoli G, Moroni M and Romano G P 2002 The determination of velocity fluctuations in shear flows by means of PTV *Proc. 12th Int. Symp. on Application of Laser Techniques to Fluid Mechanics (Lisbon)*

Haarlem B 2000 The dynamics of particles and droplets in atmospheric turbulence: a numerical study *PhD Thesis* Delft University of Technology

Hart D P 1998 The elimination of correlation errors in PIV processing *Proc. 9th Int. Symp. on the Application of Laser Anemometry to Fluid Mechanics (Lisbon)* pp 13.3.1–13.3.8

Jahne B 1997 *Digital Image Processing* (Berlin: Springer)

Keane R D and Adrian R J 1992 Theory of cross-correlation analysis of PIV images *Appl. Sci. Res.* **49** 191–215

Kim J, Moin P and Moser R 1987 Turbulence in channel flow at low Reynolds number *J. Fluid Mech.* **177** 133–66

Kobayashi T, Saga T and Sekimoto K 1989 Velocity measurement of three-dimensional flow around rotating parallel disks by digital image processing *Flow Visualization ASME-FED* vol 85 ed B Khalighi *et al* pp 29–36

Liu Z-C, Landreth C C, Adrian R J and Hanratty T J 1991 High resolution measurement of turbulent structure in a channel with particle image velocimetry *Exp. Fluids* **10** 301–12

Lucas B D and Kanade T 1981 An iterative image registration technique with an application to stereo vision *Proc. Imaging Understanding Workshop* pp 121–30

Miozzi M 2004 Particle image velocimetry using feature tracking and Delauny tessellation *Proc. 12th Int. Symp. on Application of Laser Techniques to Fluid Mechanics (Lisbon)*

Moroni M, Cardi M, Romano G P and Cenedese A 2001 Comparison between PIV and PTV in the study of near-wall turbulence *First Year Annual Report Within the European Project EUROPIV 2: A Joint Program to Improve PIV Performance for Industry and Research* Contract no G4RD-CT-2000-00190

Moroni M, Nogueira J, Miozzi M, Romano G P, Cenedese A, Rodriguez P A and Lecuona A 2004 PTV for the characterization of turbulent channel flow: comparison of experimental and simulation approaches *Particle Image Velocimetry* ed M Stanislas, J Kompenhans and J Westerweel (Berlin: Springer)

Nishio S, Sugii Y and Okuno T 2001 Analytics of PIV measurements for its higher performances *Proc. 4th Int. Symp. on Particle Image Velocimetry (Gottingen, Germany, Sept. 2001)*

Nogueira J, Lecuona A and Rodríguez P A 1999 Local field correction PIV: on the increase of accuracy of digital PIV systems *Exp. Fluids* **27** 107–16

Nogueira J, Lecuona A and Rodríguez P A 2001 Local field correction PIV, implemented by means of simple algorithms, and multigrid versions *Meas. Sci. Technol.* **12** 1911–21

Romano G P 1993 Two-point velocity measurements using LDA: spatial and temporal analysis in a turbulent boundary layer *Laser Anemometry—Advances and Application, SPIE* **2052** 597–604

Romano G P 1995 Analysis of two-point velocity measurements in near-wall flows *Exp. Fluids* **20** 68–83

Rousseeuw P J and Leroy A M 1987 *Robust Regression and Outlier Detection (Wiley Series in Probability and Mathematical Statistics)* (New York: Wiley)

Shi J and Tomasi C 1994 Good features to track *IEEE Conf. on Computer Vision and Pattern Recognition (CVPR94) (Seattle)*

Tomasi C and Kanade T 1991 Detection and tracking of point features. Shape and motion from image streams: a factorization method *Carnegie Mellon University Technical Report* CMU-CS-91-132

Udrea D D, Bryanston-Cross P J, Moroni M and Querzoli G 2000 Particle tracking velocimetry techniques *Fluid Mechanics and its Application* (Dordrecht: Kluwer) pp 279–304

Verestoy J, Chetverikov D and Nagy D 1999 Digital particle image velocimetry: a challenge for feature based tracking *Mach. Graph. Vis.* **8** 553–69

Virant M and Dracos T 1997 3D PTV and its application on Lagrangian motion *Meas. Sci. Technol.* **8** 1539–52

Westerweel J 1994 Efficient detection of spurious vectors in particle image velocimetry data *Exp. Fluids* **16** 236–47

Westerweel J 1997 Fundamentals of digital particle image velocimetry *Meas. Sci. Technol.* **8** 1379–92

Westerweel J 1998 Effect of sensor geometry on the performance of PIV *Proc. 9th Int. Symp. on Applications of Laser Techniques to Fluid Mechanics (Instituto Superior Técnico, Lisbon, Portugal)*

Westerweel J, Dabiri D and Gharib M 1997 The effect of a discrete window offset on the accuracy of cross-correlation analysis of digital PIV recordings *Exp. Fluids* **23** 20–8